Article | Open Access

Energy Materials

Mu et al. Energy Mater. 2026, 6, 600067 DOI:10.20517/energymater.2026.41

Decoupling ion/electron transport through laser-engineered vertical microchannels for high-loading solid-state lithium metal batteries

Yongbiao Mu[1,2,3], Chengjun Xu[4], Maokun Li[1], Chaozhu Huang[1,2], Zigeng Wu[1], Lin Yang[1,2], Yitian Feng[1,2], Zetao Chen[1,2], Hanshun Lai[1,2], Zhiyu Zou[1,2], Hengyuan Hu[1,2], Guobin Zhang[5], Meisheng Han[1,2,*], Liang An[3,*], Lin Zeng[1,2,*]

Keywords:
Solid-state lithium metal batteries, high-loading cathodes, mass transfer, high-voltage, laser-machining strategy

Citation: Mu, Y.; Xu, C.; Li, M.; Huang, C.; Wu, Z.; Yang, L.; Feng, Y.; Chen, Z.; Lai, H.; Zou, Z.; Hu, H.; Zhang, G.; Han, M.; An, L.; Zeng, L. Decoupling ion/electron transport through laser-engineered vertical microchannels for high-loading solid-state lithium metal batteries. *Energy Mater.* **2026**, *6*, 600067. https://dx.doi.org/10.20517/energymater.2026.41

Received: 24 Mar 2026 **First Decision:** 30 Apr 2026 **Revised:** 28 May 2026 **Accepted:** 16 Jun 2026 **Published:** 26 Jun 2026

Academic Editor: Elie Paillard
Copy Editor: Fangling Lan
Production Editor: Fangling Lan

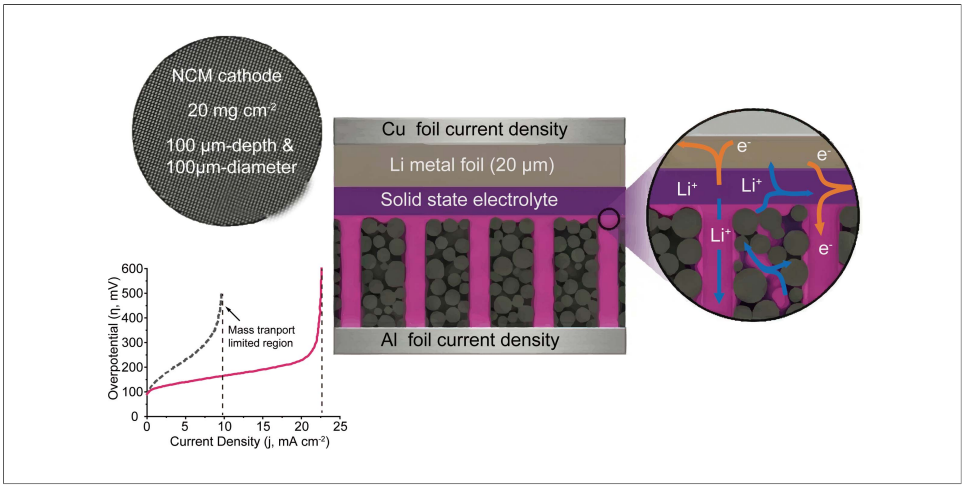

Abstract

Realizing the full potential of solid-state lithium metal batteries requires high-loading cathodes; however, their practical implementation is fundamentally hindered by sluggish mass transport and severe polarization arising from highly tortuous ion-diffusion pathways. Herein, we report a scalable three-dimensional (3D) composite architecture that decouples ion and electron transport through laser-engineered vertical microchannels. By uniformly infiltrating a solid polymer electrolyte into these directional channels within a thick $LiNi_{0.8}Co_{0.1}Mn_{0.1}O_2$ cathode, the tortuous diffusion bottlenecks inherent to conventional electrodes are effectively alleviated. Spatiotemporal multiphysics simulations, together with operando impedance analysis, reveal that this 3D architecture markedly reduces mass-transfer resistance and mitigates localized concentration polarization. As a result, the integrated cathode delivers highly reversible redox chemistry, enabling stable cycling over a high-voltage window of up to 4.5 V and excellent rate capability up to 5.0 C. To further demonstrate its practical relevance, a prototype single-layer solid-state pouch cell based on this architecture achieves a stable capacity of 95 mAh with high Coulombic efficiency.

[1]Shenzhen Key Laboratory of Advanced Energy Storage, Department of Mechanical and Energy Engineering, Southern University of Science and Technology, Shenzhen 518055, Guangdong, China.
[2]SUSTech Energy Institute for Carbon Neutrality, Southern University of Science and Technology, Shenzhen 518055, Guangdong, China.
[3]Department of Mechanical Engineering, The Hong Kong Polytechnic University, Kowloon 999077, Hong Kong, China.
[4]School of Energy Science and Engineering, Nanjing Tech University, Nanjing 210000, Jiangsu, China.
[5]College of New Materials and New Energies, Shenzhen Technology University, Shenzhen 518118, Guangdong, China.

*Correspondence to: Dr. Meisheng Han, Department of Mechanical and Energy Engineering, Southern University of Science and

Technology, No. 1088 Xueyuan Avenue, Nanshan District, Shenzhen 518055, Guangdong, China. E-mail: hanms@sustech.edu.cn; Prof. Liang An, Department of Mechanical Engineering, The Hong Kong Polytechnic University, Hung Hom, Kowloon 999077, Hong Kong, China. E-mail: liang.an@polyu.edu.hk; Prof. Lin Zeng, Department of Mechanical and Energy Engineering, Southern University of Science and Technology, No. 1088 Xueyuan Avenue, Nanshan District, Shenzhen 518055, Guangdong, China. E-mail: zengl3@sustech.edu.cn

This laser-patterning strategy offers a broadly applicable route to overcoming fundamental mass-transport limitations in thick solid-state cathodes, thereby accelerating the development of high-energy-density solid-state batteries.

INTRODUCTION

Solid-state lithium metal batteries (SSLMBs) are widely recognized as a promising route toward high-energy-density and intrinsically safe energy storage. To surpass commercial lithium-ion batteries at the practical cell level, SSLMBs must employ thick, high-loading cathodes (e.g., areal capacities > 4 mAh cm^{-2}) to maximize the fraction of electrochemically active material[1-3]. However, when transitioning from thin-film model systems to practically relevant thick solid-state electrodes, a pronounced gap emerges between theoretical expectations and actual electrochemical performance, with both achievable energy density and rate capability falling far short of their projected limits[4-7].

This discrepancy primarily arises from sluggish mass-transport kinetics in conventional solid polymer electrolytes (SPEs) and composite cathodes. In unpatterned thick electrodes, the randomly percolated network of densely packed active particles (e.g., $LiNi_{0.8}Co_{0.1}Mn_{0.1}O_2$ (NCM811)) creates highly tortuous and convoluted diffusion pathways for lithium ions (Li^+)[8-10]. Consequently, ion and electron transport become strongly coupled and mutually constrained. Under practical current densities, such severe tortuosity generates substantial through-plane mass-transfer resistance and causes rapid Li^+ depletion at the deep electrode/electrolyte interface, thereby inducing pronounced localized concentration polarization[11-13]. As a result, only the superficial region of the cathode remains electrochemically active, leading to premature cell polarization, poor rate performance, and rapid capacity decay. Recent efforts to address these limitations have been hindered by trade-offs[14-16]. For example, the use of highly porous three-dimensional metal or carbon scaffolds as current collectors can facilitate electrolyte infiltration, but substantially increases the inactive mass fraction and correspondingly lowers the overall volumetric energy density. Alternatively, sacrificial-template approaches (e.g., freeze-casting) used to construct porous cathode architectures often compromise active-material packing density and structural integrity, resulting in mechanically fragile electrodes[17-19]. Furthermore, extensive plasticization of SPEs with solvents to improve bulk ionic conductivity inevitably reduces their mechanical modulus, making them more susceptible to lithium dendrite penetration. Therefore, existing strategies have not successfully resolved the fundamental through-plane transport bottleneck without introducing considerable manufacturing complexity or sacrificing device-level energy density[20,21].

To fundamentally overcome this kinetic limitation, we propose a scalable three-dimensional integrated composite architecture that decouples ion and electron transport within high-loading solid-state cathodes. Specifically, highly ordered vertical microchannel arrays are directly introduced into dense NCM811 electrodes by precision laser machining[22]. Subsequent infiltration of these microchannels with an SPE establishes a decoupled transport framework: the densely packed active-material matrix provides a continuous electronically conductive network, while the polymer-filled vertical channels act as direct, ultra-low-tortuosity pathways for rapid through-plane Li^+ transport[23-27]. By integrating spatiotemporal multiphysics simulations with operando distribution of relaxation times (DRT) analysis, we reveal the kinetic advantages of this 3D architecture, including the markedly suppression of concentration polarization and markedly accelerated interfacial redox kinetics. Freed from the mass-transfer limitations inherent to

conventional thick cathodes, the integrated three-dimensional (3D) cathode exhibits outstanding structural and electrochemical reversibility. It delivers stable cycling over an extended voltage window of 2.7-4.5 V and exceptional rate capability up to 5.0 C, performance that is difficult to achieve with conventional thick SSLMB cathodes. We further demonstrate the practical relevance of this laser-engineered strategy by assembling a 95 mAh single-layer solid-state pouch cell, which exhibits stable cycling and high Coulombic efficiency under demanding operating conditions. Overall, this architecture offers a scalable and broadly applicable strategy for overcoming the mass-transport limitations of thick solid-state electrodes, thereby bridging the gap between theoretical material potential and practical deployment in high-energy-density devices.

EXPERIMENTAL

Materials

Commercial pristine $LiNi_{0.8}Co_{0.1}Mn_{0.1}O_2$ (NCM811) powder was purchased from Guangdong Canrd New Energy Technology Co., Ltd. (China). Poly(vinylidene fluoride) (PVDF, 5140), triethyl phosphate (TEP, > 99.8%), and lithium bis(fluorosulfonyl)imide (LiFSI, 99.9%) were obtained from Sigma-Aldrich. Super P carbon black and battery-grade aluminum foil (15 μm thick) were supplied by Guangdong Canrd New Energy Technology Co., Ltd. (China). Lithium metal foil (50 μm thick) and aluminium-plastic films for pouch-cell assembly were purchased from Shenzhen Kejing Star Technology Co., Ltd. (China). All chemicals were used as received without further purification. Moisture-sensitive materials were stored and handled in an argon-filled glovebox (O_2 < 0.01 ppm, H_2O < 0.01 ppm).

Fabrication of the NCM electrode

The conventional unpatterned NCM composite cathodes were fabricated by a standard slurry-casting process. NCM811 active material, Super P conductive carbon, and PVDF binder were mixed at a weight ratio of 96:2:2 and dispersed in N-methyl-2-pyrrolidone (NMP) to form a homogeneous slurry. The resulting slurry was cast onto commercial aluminum foil current collectors using a doctor blade, followed by drying in a vacuum oven at 110 °C for 12 h to remove residual NMP. After drying, the electrodes were calendared to achieve the desired porosity and a high areal mass loading of approximately 18.9 mg cm^{-2}. To compensate for laser-induced mass loss and match the loading of the conventional electrode, 25 mg cm^{-2} cathode sheets were prepared prior to laser processing [Supplementary Table 1].

Fabrication of the 3D patterned NCM electrode

To construct the vertical microchannel arrays, the pristine high-loading NCM cathodes were processed using a femtosecond laser ablation system (Tangerine, Amplitude, France). The laser parameters were carefully optimized to ensure complete penetration of the thick composite electrode while avoiding damage to the underlying aluminum current collector. Specifically, a laser wavelength of 1,030 nm, a repetition rate of 100 kHz, and an output power of 5 W were used. The resulting 3D-patterned NCM electrodes were then cleaned with compressed argon gas to remove ablation debris and dried under vacuum prior to electrolyte infiltration.

Fabrication of the polymer electrolyte

The formulation of this solid polymer electrolyte (SPE) was developed based on our group's previously reported work[28], with further optimization of the solvents. Specifically, a predetermined amount of lithium bis(fluorosulfonyl)imide (LiFSI) was dissolved in a binary solvent mixture of triethyl phosphate (TEP) and dimethylformamide (DMF) with a mass ratio of 3:7 (wt/wt). To this solution, the electrolyte precursor was prepared using 1.0 g PVDF, 0.8 g LiFSI, and 8.0 g mixed solvent with a TEP/DMF mass ratio of 3:7. Therefore, the masses of TEP and DMF were 2.4 and 5.6 g, respectively. The polymer content in the precursor solution was 10.2 wt%, and the LiFSI content was 8.2 wt%. The LiFSI concentration in the

TEP/DMF mixed solvent was approximately 0.52 M, and the molar ratio of PVDF repeating units to Li^+ was approximately 3.65:1. Specifically, the PVDF polymer matrix was added. The mixture was continuously stirred at 60 °C for 6 h within an argon-filled glovebox (H_2O < 0.1 ppm, O_2 < 0.1 ppm) to ensure the formation of a homogeneous, transparent, and viscous precursor. Subsequently, the precursor solution was cast onto a clean glass substrate using a doctor blade with a controlled wet film thickness of 50 μm. To ensure complete solvent removal and membrane crystallization, the as-cast films were transferred to a vacuum oven and dried at 80 °C for 24 h. The resulting free-standing SPE membranes were then harvested for further electrochemical characterization.

Fabrication of the 3D NCM/electrolyte electrode

The seamless integration of the SPE with the 3D-patterned NCM framework was achieved through direct infiltration followed by in situ solidification. The as-prepared viscous SPE precursor was uniformly cast onto the surface of the laser-ablated 3D NCM cathode. The casting process was performed on a heating stage maintained at 60 °C, which ensured the optimal fluidity of the polymer electrolyte solution for superior infiltration into the microstructures. To ensure complete penetration of the polymer electrolyte into the deep vertical microchannels and interstitial voids among the active particles, the electrode was subjected to vacuum infiltration at room temperature for 30 min. Subsequently, the electrode was thermally treated at 80 °C for 24 h to remove residual volatile species and form a robust, fully integrated 3D composite cathode. Finally, the obtained SPE/NCM811 composite cathode still contains a small amount of residual solvent species (< 15%), while no liquid electrolyte or flowable solvent exists in the composite electrode.

Fabrication and testing of solid-state pouch cells

To evaluate the practical applicability of the 3D integrated architecture, single-layer solid-state pouch cells were assembled in an argon-filled glovebox. The integrated 3D NCM/SPE cathode was cut into a rectangular dimension of 75 mm × 60 mm. A lithium metal foil (50 μm thick) with matching dimensions was used as the anode. The cathode and anode were carefully stacked with the integrated SPE layer serving as the separator. Nickel and aluminum tabs were ultrasonically welded to the anode and cathode current collectors, respectively. The assembled cell stack was then enclosed in a commercial aluminium-plastic film and hermetically sealed under high vacuum (-0.09 MPa) using a compact vacuum sealer (Kejing/MTI Corporation). The designed capacity of the resulting pouch cell was 95 mAh.

Electrochemical characterization

Galvanostatic charge-discharge (GCD) measurements of both coin cells (CR2032 type) and pouch cells were performed using a multichannel battery testing system (Neware, China) over a voltage window of 2.7-4.5 V (*vs*. Li/Li^+). All electrochemical tests were conducted in a temperature-controlled chamber at 30 °C. The C-rates were calculated on the basis of the theoretical capacity of NCM811 (1 C = 200 mA g^{-1}). Cyclic voltammetry (CV) and operando electrochemical impedance spectroscopy (EIS) measurements were carried out using an electrochemical workstation (Bio-Logic, France). CV curves were recorded at scan rates ranging from 0.1 to 1.0 mV s^{-1}. EIS spectra were collected over a frequency range of 10^5 Hz to 10^{-2} Hz with an AC amplitude of 10 mV. Distribution of relaxation times (DRT) analysis was performed by computational deconvolution of the Nyquist plots using a ridge-regression algorithm to resolve and quantify the individual polarization processes. The galvanostatic intermittent titration technique (GITT) was employed to evaluate the Li^+ diffusion kinetics of the NCM811 cathode. The measurements were conducted after three formation cycles at 0.1 C. During the GITT test, a constant-current pulse corresponding to 0.1 C was applied for 30 min, followed by a relaxation period of 2 h to allow the cell voltage to reach a quasi-open-circuit state. This pulse-relaxation sequence was repeated within the voltage range of 2.8-4.5 V.

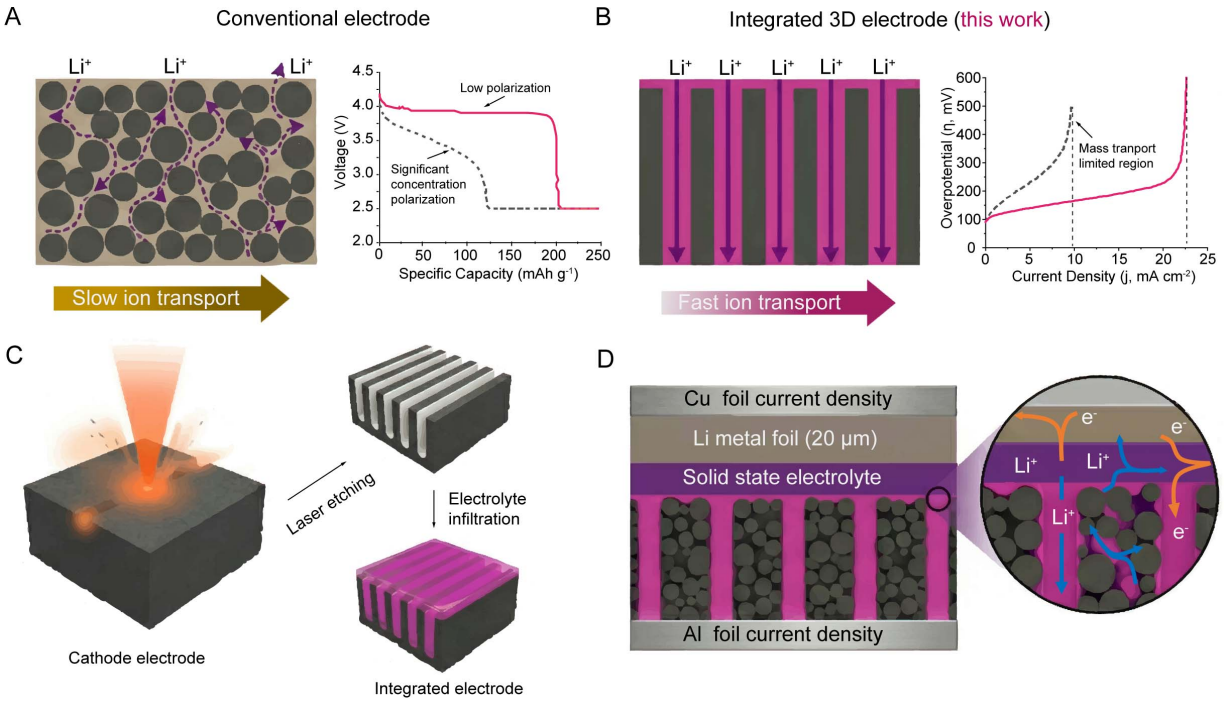

Figure 1. Design of the integrated 3D solid-state electrode. (A and B) Transport kinetics and electrochemical profiles of a conventional thick cathode (A) versus the integrated 3D electrode featuring vertical channels (B). (C) Fabrication via laser etching and polymer electrolyte infiltration. (D) Cross-section of the solid-state cell, illustrating decoupled Li^+ and electron transport pathways.

RESULTS AND DISCUSSION

Rational design and structural realization of the 3D integrated cathode

The practical performance of thick solid-state cathodes is fundamentally limited by sluggish mass transport arising from the highly tortuous diffusion pathways within randomly packed active materials. As illustrated in Figure 1A, conventional unpatterned architectures force lithium ions (Li^+) to traverse a convoluted transport network within the SPE. Such structural tortuosity imposes a substantial kinetic penalty, as the rapid buildup of concentration polarization leads to premature voltage decay and consequently restricts the accessible specific capacity. To overcome these mass-transfer limitations, we developed an integrated 3D composite cathode incorporating vertical microchannels [Figure 1B]. This rationally designed architecture creates direct, low-tortuosity pathways for rapid Li^+ transport, thereby expanding the mass-transport boundary of the electrode. The kinetic advantage of this design is clearly manifested in the overpotential response. Whereas conventional electrodes exhibit a sharp increase in overpotential even at relatively low current densities because of severe concentration gradients, the 3D integrated architecture maintains low and stable polarization under high-flux operating conditions. The origin of this enhanced electrochemical behavior lies in the spatial decoupling of ion and electron-transport pathways. As shown in Figure 1C, the integrated cathode architecture was constructed by precision laser ablation of the pristine NCM811 cathode, followed by conformal infiltration of the SPE into the resulting vertical microchannels. The corresponding microstructural schematic [Figure 1D] illustrates that the dense NCM811 framework retains a continuous percolation network for electron (e^-) transport, whereas the SPE-filled laser-ablated channels provide dedicated pathways for Li^+ conduction. By spatially decoupling electronic and ionic transport within the thick solid-state cathode, this architecture effectively mitigates the intrinsic transport competition between electron continuity and ion accessibility.

We systematically monitored the morphological evolution of the electrode to verify the structural fidelity of the 3D architecture. As a baseline, the unpatterned high-loading NCM811 thick cathode was first characterized. Planar and cross-sectional SEM images [Supplementary Figures 1 and 2] show a pristine

active-layer thickness of approximately 100 μm, with a random yet densely compact particle arrangement. The corresponding EDS elemental maps further confirm the homogeneous distribution of Ni, Co, Mn, and O throughout the unmachined electrode matrix [Supplementary Figure 3]. Although such a densely packed morphology with a thickness of ~100 μm ensures continuous electronic percolation, it intrinsically hinders efficient through-plane ion transport, thereby imposing severe mass-transfer limitations.

To address this bottleneck, a femtosecond laser was employed to reconstruct the pristine electrode architecture. Optical images of both sides of the patterned electrode confirm that the microchannels penetrate the entire thickness of the cathode coating [Supplementary Figure 4]. Three-dimensional confocal microscopy and SEM observations [Figure 2A-E] further reveal a highly uniform microchannel array within the NCM811 cathode, with both the pore diameter and interpore spacing precisely controlled at approximately 100 μm [Supplementary Figure 5]. High-magnification SEM images show that the NCM material surrounding the laser-drilled channels remains structurally intact, indicating that the laser-processing procedure does not compromise the intrinsic capacity-delivery capability of the active material [Supplementary Figure 6]. To further verify the structural and chemical integrity of the laser-patterned cathode, we supplemented XRD and XPS characterizations. The XRD results show no obvious phase change after laser processing [Supplementary Figure 7], while the XPS spectra confirms that the surface chemical states of Ni, Mn, and O remain largely unchanged [Supplementary Figure 8]. These results indicate that the optimized laser-ablation process does not cause significant thermal damage to the NCM811 cathode. To further evaluate structural uniformity, confocal surface profiling was performed [Supplementary Figure 9]. The results demonstrate that the vertical microchannels fully penetrate the electrode matrix, with a depth comparable to the electrode thickness (~100 μm). The periodic array exhibits high structural fidelity, with a well-defined pore diameter of 100 μm and an interpore spacing of 100 μm. This high-density channel arrangement serves an important engineering function by providing the framework for constructing a continuous 3D polymer-electrolyte network, while simultaneously facilitating the wetting and deep infiltration of highly viscous electrolyte precursors at multiple sites throughout the electrode. Notably, despite the localized intensity of the ablation process, the surrounding unmachined active material remains structurally preserved. Consistently, planar and cross-sectional EDS maps of the patterned electrode [Figure 2F-I and Supplementary Figure 10] show the same uniform distribution of Ni, Co, Mn, and O as that of the pristine electrode, confirming that the laser reconstruction process is chemically non-destructive.

With the 3D structural framework established, a PVDF-based solid polymer electrolyte was introduced as the ion-conducting medium based on our previous report[28]. To ensure efficient electrolyte infiltration and rapid ionic conduction within the thick 3D-patterned electrodes, the solvent system was systematically optimized. Specifically, a binary mixture of TEP and DMF with a mass ratio of 3:7 was developed. This optimized formulation was strategically designed to achieve a synergistic balance between high-voltage oxidative stability and enhanced ionic conductivity[2,29]. To elucidate its internal coordination environment, Fourier transform infrared (FTIR) and Raman spectra were collected [Supplementary Figures 11 and 12]. The formation of $[TEP\text{-}Li]^+$ coordination complexes is clearly evidenced by FTIR spectroscopy, as indicated by the characteristic shift of the P=O···Li^+ stretching band at 1,260 cm^{-1}. Raman spectral deconvolution further reveals a distinct Li^+ coordination environment in the PVDF-based SPE, dominated by contact ion pairs (CIPs) and aggregates (AGGs). The absence of solvent-separated ion-pair (SSIP) signals suggests that residual TEP molecules are effectively incorporated into the Li^+ solvation sheath. Taken together, the FTIR and Raman results indicate a solvation structure primarily governed by FSI^- anions, with localized contributions from coordinated TEP molecules. Such a coordination environment is advantageous for modulating the solvation sheath and promoting lithium-ion transport. This optimized network translates into high ionic conductivity. Electrochemical impedance spectroscopy [Supplementary Figure 13] gives a room-temperature ionic conductivity of 1.36 mS cm^{-1}, which is sufficient to support rapid ion transport in

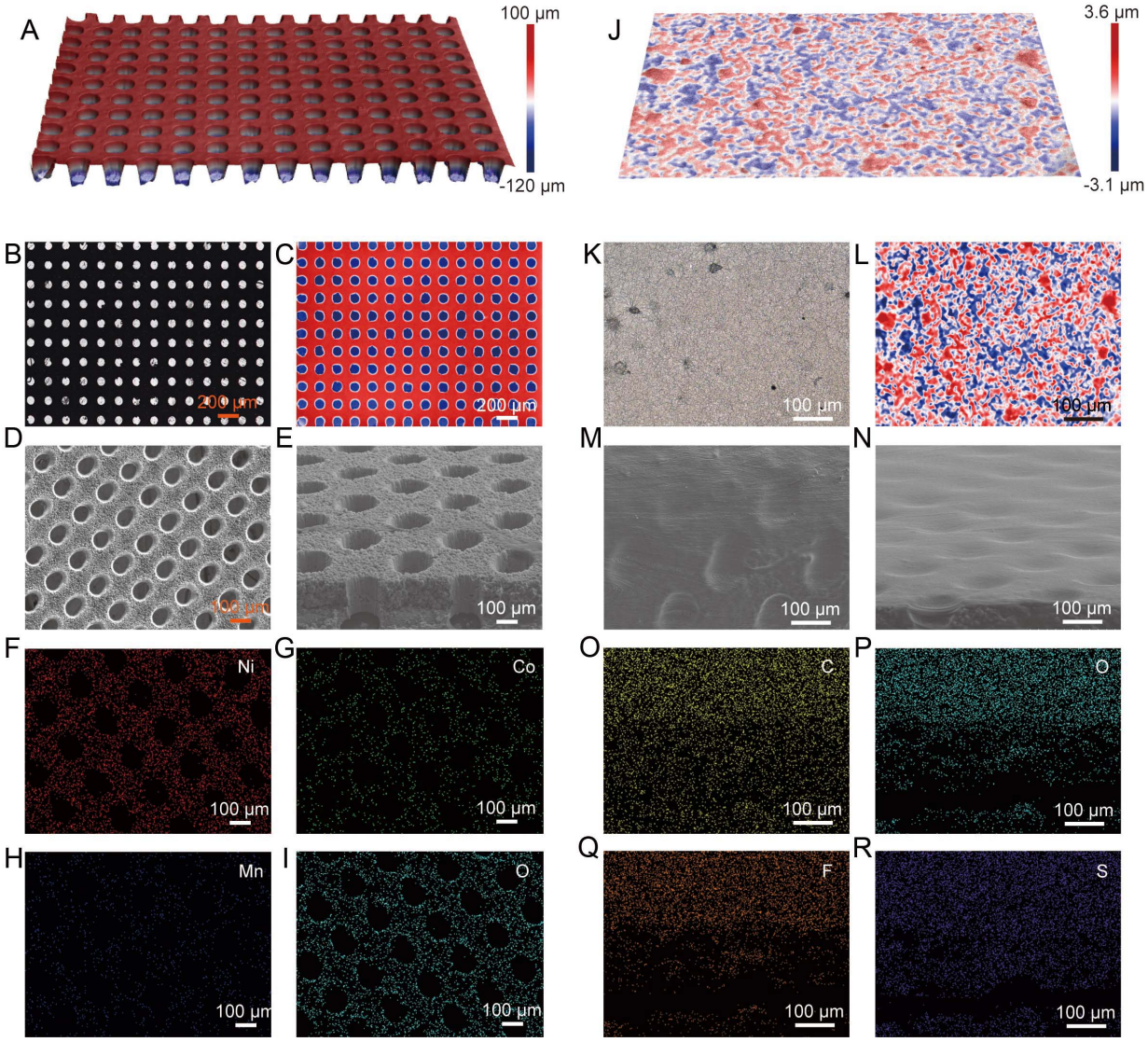

Figure 2. Structural and elemental characterization of the integrated 3D electrode. (A-E) 3D profilometry (A), optical (B and C), and SEM (D and E) images of the bare laser-machined NCM811 cathode, revealing a uniform vertical microchannel array. (F-I), Corresponding EDS elemental maps of Ni, Co, Mn, and O. (J-N), 3D profilometry (J), optical (K and L), and SEM (M and N) images of the composite cathode after solid polymer electrolyte infiltration, demonstrating complete channel filling. (O-R) Corresponding EDS maps of C, O, F, and S elements.

thick electrodes. In addition, linear sweep voltammetry (LSV, Supplementary Figure 14) and electrochemical floating tests [Supplementary Figure 15] show that the oxidation stability of the SPE extends to 5.0 V (*vs*. Li/Li^+), providing an adequate electrochemical stability window for the high-voltage NCM811 cathode. The interfacial compatibility and dendrite-suppression capability of the SPE toward lithium metal were further evaluated in Li||Li symmetric cells [Supplementary Figure 16]. The cell exhibited stable cycling for more than 500 h at 0.2 mA cm^{-2} with a low and steady overpotential, indicating that the SPE can effectively suppress the growth and penetration of lithium dendrites.

Building on the validated electrolyte properties, the PVDF-based electrolyte was integrated into the laser-structured electrodes through a combined casting and vacuum-infiltration process. Three-dimensional confocal microscopy and SEM images [Figure 2J-N] show that the polymer completely fills and covers the microchannels due to the high solubility of both PVDF polymer and LiFSI in DMF solvent

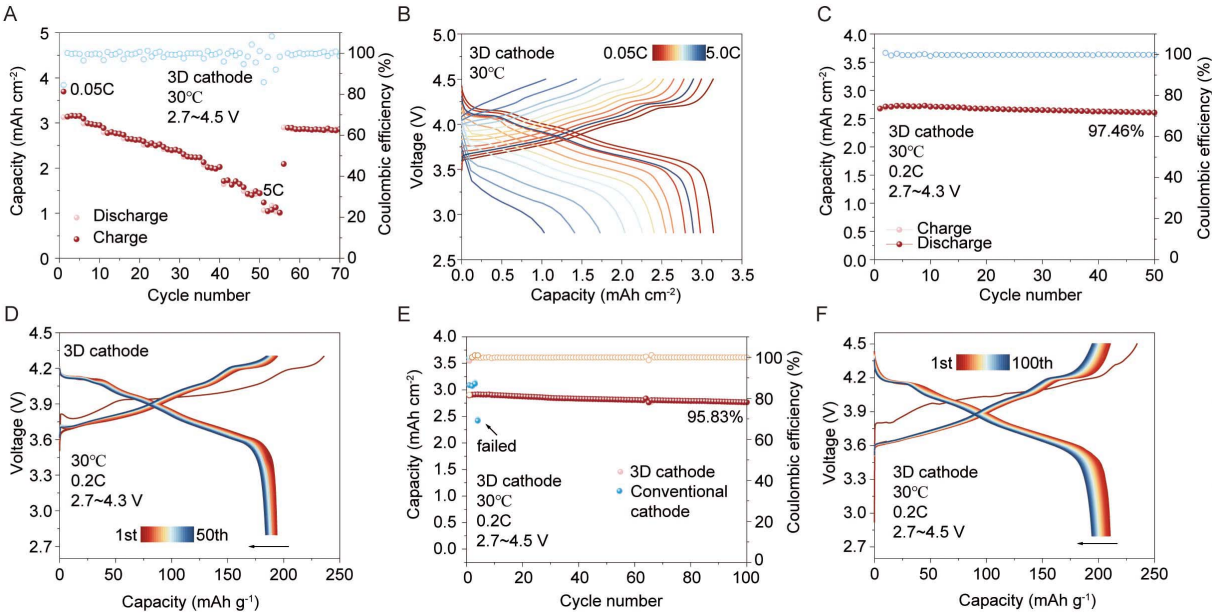

Figure 3. Electrochemical performance of the integrated 3D electrode. (A and B) Rate capability (A) and corresponding charge-discharge profiles (B) of the 3D cathode at various rates from 0.05 C to 5.0 C (2.7-4.5 V). (C and D) Cycling stability of the 3D cathodes (C) and voltage profiles (D) at 0.2 C within a standard voltage window of 2.7-4.3 V. (E and F) Comparative cycling performance of the 3D and conventional cathodes (E) and voltage profiles of the 3D cathode (F) under an extended high-voltage window (2.7-4.5 V) at 0.2 C. All tests were conducted at 30 °C.

[Supplementary Figure 17] Notably, the solidified composite electrode surface develops a distinct Turing-like structure [Supplementary Figure 18]. This self-organized micro-/nanostructured topography markedly increases the electrochemically active interfacial area and provides a favorable physical environment for homogenizing interfacial ion flux. Topographic analysis further clarifies the surface morphology after electrolyte casting [Supplementary Figure 19]. The results clearly show that the pre-engineered vertical microchannels are completely filled with the solid polymer electrolyte. The integrated electrode exhibits a highly planar surface, without discernible depressions, protrusions, or other structural irregularities arising from electrolyte shrinkage. Planar EDS mapping [Supplementary Figure 20] further confirms the dense and uniform coverage of the surface polymer layer. Examination of the electrode interior, including cross-sectional EDS maps of Ni, Co, Mn, C, O, F, and S [Figure 2O-R and Supplementary Figure 21] together with cross-sectional SEM images [Supplementary Figure 18], demonstrates that the polymer electrolyte uniformly penetrates to the bottom of the ablated channels. This seamless physical interlocking, extending from the surface Turing-like morphology deep into the vertical microchannels, confirms the formation of robust 3D interfacial contact throughout the entire ~100 μm thickness of the electrode.

Electrochemical performance under demanding conditions

The electrochemical performance of the decoupled 3D architecture was evaluated at exceptionally high cathode mass loadings. The integrated 3D cathode exhibits excellent rate capability over a wide voltage window of 2.7-4.5 V [Figure 3A and B]. At 0.05 C, the initial areal capacity reaches approximately 3.2 mAh cm^{-2}, and a capacity of ~1.2 mAh cm^{-2} is still maintained even at an ultrahigh rate of 5.0 C. The corresponding charge-discharge profiles [Figure 3B] display relatively flat voltage plateaus, indicative of low polarization and fast interfacial kinetics. These results suggest that the directional ion-transport channels effectively suppress localized Li^+ depletion even under high-flux operating conditions. In contrast, conventional unpatterned thick electrodes with the same mass loading suffer from severe mass-transfer limitations and fail to operate even at a relatively low rate of 0.2 C [Supplementary Figure 22].

The 3D cathode also demonstrates stable long-term cycling performance. When cycled at 0.2 C within a conventional voltage window of 2.7-4.3 V, it retains a highly reversible areal capacity of ~2.7 mAh cm^{-2} over 50 cycles, with an average Coulombic efficiency of 99.32% [Figure 3C and D]. The corresponding voltage profiles further confirm the low polarization and improved interfacial reaction kinetics. By comparison, the cycling data in Supplementary Figure 23 show that conventional thick electrodes undergo rapid capacity decay at 4.3 V, while their voltage profiles reveal severe polarization that progressively intensifies during cycling [Supplementary Figure 24]. To further probe the kinetic limits of the system, cycling tests were extended to a more stringent high-voltage window of 2.7-4.5 V at 0.2 C [Figure 3E and F]. Under these conditions, the conventional cathodes fail catastrophically within the first five cycles, owing to uncontrolled localized overpotentials and rapid interfacial degradation[30]. As the upper cutoff voltage is increased to 4.5 V, the polarization of the control electrode rises sharply [Supplementary Figure 25], leading to a sudden capacity drop and eventual loss of charge-storage capability. In contrast, the integrated 3D cathode maintains stable operation for 100 cycles, delivering a reversible areal capacity of ~2.8 mAh cm^{-2} with a Coulombic efficiency of 95.83%. The incorporation of TEP extends the electrochemical stability window of the PVDF-based electrolyte. TEP serves as a crucial high-voltage stabilizer and effectively suppresses the oxidative decomposition of the electrolyte at the high-voltage cathode interface, thereby ensuring stable cycling of the NCM cathode[31]. Compared with recently reported solid-state battery systems, the Li||3D SPE/NCM811 cell exhibits favorable cycling stability under high-loading and high-voltage conditions [Supplementary Table 2]. This pronounced performance difference provides strong evidence that the 3D architecture effectively mitigates destructive localized polarization by accelerating mass transport.

Elucidating decoupled transport kinetics and mitigated polarization

Spatiotemporal multiphysics simulations were performed to map the evolution of Li^+ concentration and thereby elucidate the physical origin of the observed electrochemical behavior [Supplementary Figure 26]. In conventional thick electrodes, the deeper regions are located far from the bulk electrolyte membrane and lack efficient fast-ion-transport pathways. As a result, through-plane ion penetration is severely hindered, leading to the development of a pronounced concentration gradient within the electrode. This mass-transfer limitation drives the bottom electrode/electrolyte interface into severe Li^+ depletion ($< 0.5 \times 10^4$ mol m^{-3}) within only 100 s [Figure 4A]. In contrast, the integrated 3D cathode exhibits fundamentally different transport behavior [Figure 4B]. Its penetrated polymer-electrolyte network functions as a series of ionic highways, allowing Li^+ within the cathode particles to travel only short distances before reaching adjacent electrolyte channels[32,33]. The substantially shortened diffusion pathways effectively homogenize the internal Li^+ distribution and suppress concentration polarization. This improved transport characteristic provides the kinetic foundation for the superior rate capability and cycling stability of the 3D architecture. Consistent with these results, post-cycling SEM images of the NCM/SPE cathode and Li metal anode show that the integrated 3D interface remains structurally intact without obvious degradation [Supplementary Figures 27 and 28]. Such morphological robustness is essential for sustaining high ionic conductivity and low interfacial resistance during prolonged cycling. Furthermore, interfacial SEM images of the cycled NCM811 cathode taken from different views [Supplementary Figure 29] show that the cathode morphology is well preserved after cycling. The polymer electrolyte remains in intimate contact with the electrode, and the overall electrode structure remains intact without obvious structural collapse. XPS depth-profiling analysis of the cycled SPE/NCM811 composite cathode, including C 1s, P 2p, and F 1s spectra, is shown in Supplementary Figure 30. The results reveal the presence of organic species as well as P- and F-rich inorganic fragments on the surface of the cycled composite electrode. This indicates the formation of a passivating interfacial layer during cycling, which is beneficial for stabilizing the electrode interface and promoting ions transport.

Operando EIS combined with distribution of relaxation times (DRT) analysis was employed to track the evolution of internal resistance and interfacial processes throughout an entire charge-discharge cycle

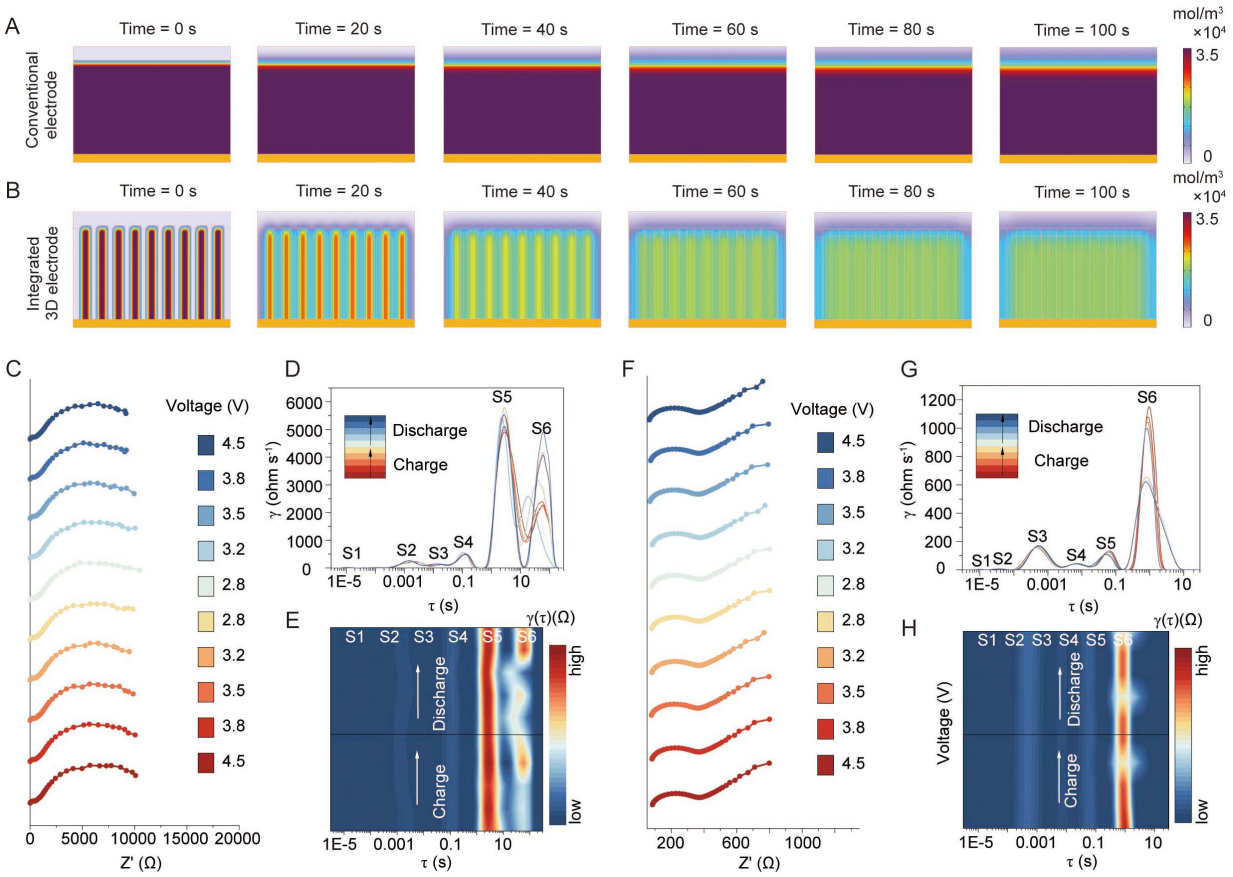

Figure 4. Mass transport simulations and operando kinetic analysis. (A and B) Simulated spatiotemporal evolution of Li^+ concentration in the conventional (A) and integrated 3D (B) electrodes. (C-H) Operando electrochemical impedance spectroscopy (EIS) during charge and discharge: Nyquist plots, distribution of relaxation times (DRT) profiles, and 2D DRT contour maps for the conventional (C-E) and integrated 3D (F-H) electrodes, demonstrating drastically reduced impedance and accelerated interfacial kinetics in the 3D architecture.

[Figure 4C-H]. Deconvolution of the DRT spectra enables the complex impedance response to be resolved into distinct physicochemical processes. Peak S1 (~10^{-4} s) is associated with bulk ionic conduction in the polymer electrolyte and electronic contact resistance. Peaks S2 and S3 (10^{-3} to 10^{-2} s) correspond to mass-transport resistance across the solid electrolyte interphase (SEI) and cathode electrolyte interphase (CEI), respectively. Peak S4 (~10^{-1} s) is assigned to charge-transfer kinetics, whereas S5 (1-10 s) originates from solid-state Li^+ diffusion within the NCM811 lattice. Finally, S6 (> 10 s) is attributed to macroscopic concentration polarization. The conventional cathode exhibits a large and highly unstable overall impedance, fluctuating between 5,000 and 20,000 Ω during cycling [Figure 4C-E]. In the corresponding DRT profiles [Figure 4D], peaks S2-S6 appear broad, irregular, and poorly resolved, with their positions shifting markedly as a function of the state of charge and discharge. The associated two-dimensional DRT contour map [Figure 4E] further visualizes these pronounced fluctuations throughout the entire cycle. Such persistent impedance instability indicates continuous interfacial degradation and severely hindered electrochemical kinetics.

By contrast, the integrated 3D cathode reduces the overall electrode impedance by more than one order of magnitude, stabilizing it within the range of 200-400 Ω. DRT analysis further confirms the superior interfacial stability of this architecture [Figure 4F-H]. As shown in Figure 4G, peaks S1-S4 remain at nearly fixed positions and maintain very low intensities throughout the entire cycle. The corresponding two-dimensional DRT contour map [Figure 4H] directly visualizes this remarkable stability over the full

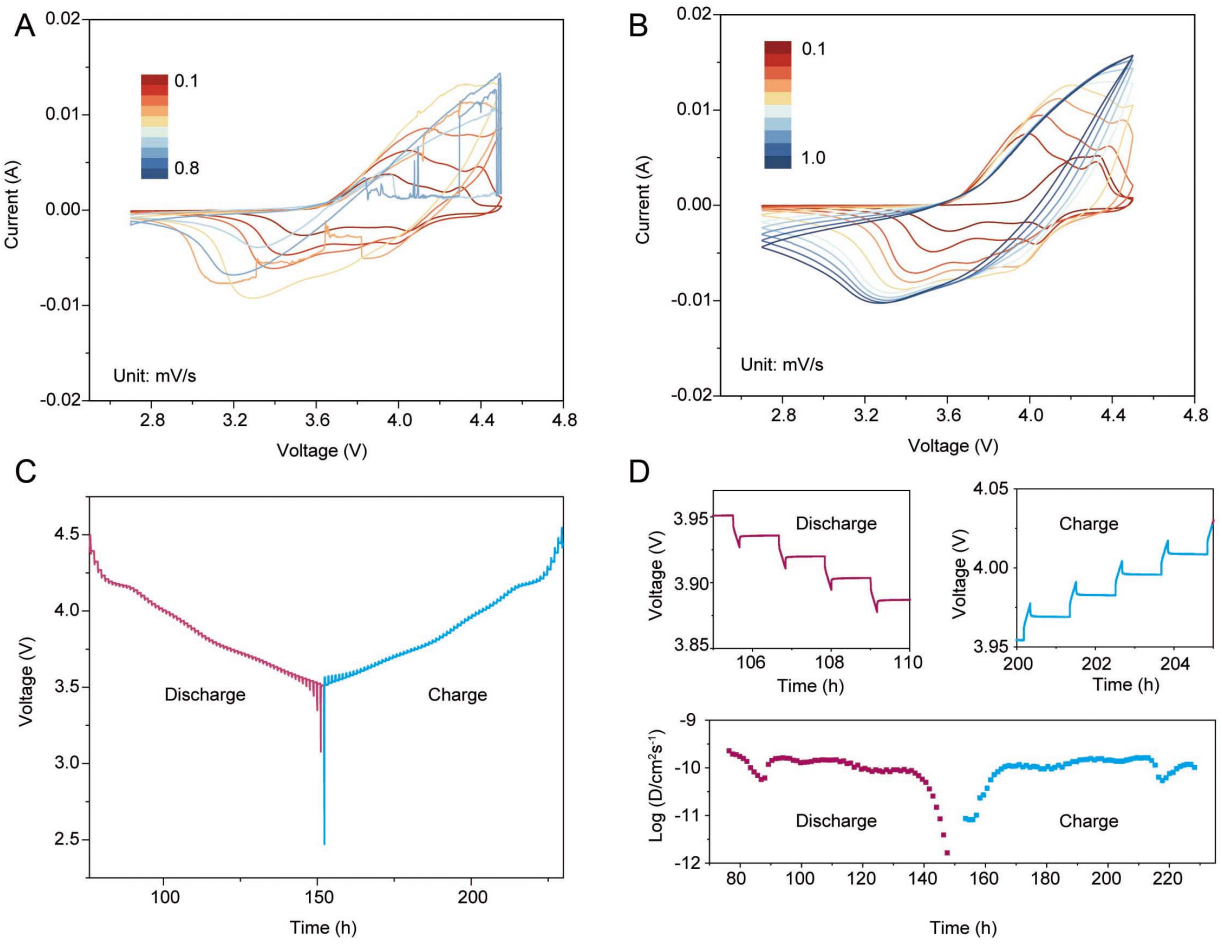

Figure 5. Electrochemical kinetics and redox reversibility. (A and B) Cyclic voltammetry (CV) curves of the conventional (A) and integrated 3D (B) electrodes at various scan rates, demonstrating superior redox reversibility and enhanced reaction kinetics in the 3D architecture. (C) Galvanostatic intermittent titration technique (GITT) profiles of the integrated 3D electrode, illustrating the equilibrium potential and overpotential during the dynamic processes. (D) Corresponding localized magnification of GITT curves during the discharge and charge processes, along with the calculated lithium-ion diffusion coefficients (D_{Li^+}) as a function of the state of charge/discharge.

operando timescale. These results indicate that the 3D architecture establishes a robust and persistent physical interface, effectively suppressing continuous degradation and excessive thickening of the CEI and SEI layers. Although peaks S5 and S6 still show expected fluctuations near the end of charge and discharge, owing to the intrinsic thermodynamic limitations of solid-state diffusion under deep delithiation/lithiation conditions[34,35], their absolute intensities remain substantially lower than those of the control electrode. This operando evolution demonstrates that the 3D transport network not only enables rapid spatial ion transport but also preserves a stable electrochemically active interface throughout the reaction process.

To further elucidate the electrochemical kinetics and redox reversibility, CV and GITT measurements were systematically performed. As shown in Figure 5A, the conventional thick cathode exhibits pronounced voltage polarization and disordered current fluctuations as the scan rate increases to 0.8 mV s^{-1}, clearly indicating sluggish mass transport within the tortuous NCM811 matrix. In sharp contrast, the 3D integrated electrode [Figure 5B] retains symmetric and well-defined redox peaks even at a higher scan rate of 1.0 mV s^{-1}, demonstrating markedly improved reaction kinetics and excellent structural reversibility.

The through-plane ion-transport kinetics were further quantified by GITT measurements [Figure 5C], which show a stable evolution of the equilibrium potential together with markedly reduced overpotential throughout cycling. Enlarged GITT profiles [Figure 5D] further reveal rapid voltage relaxation and a

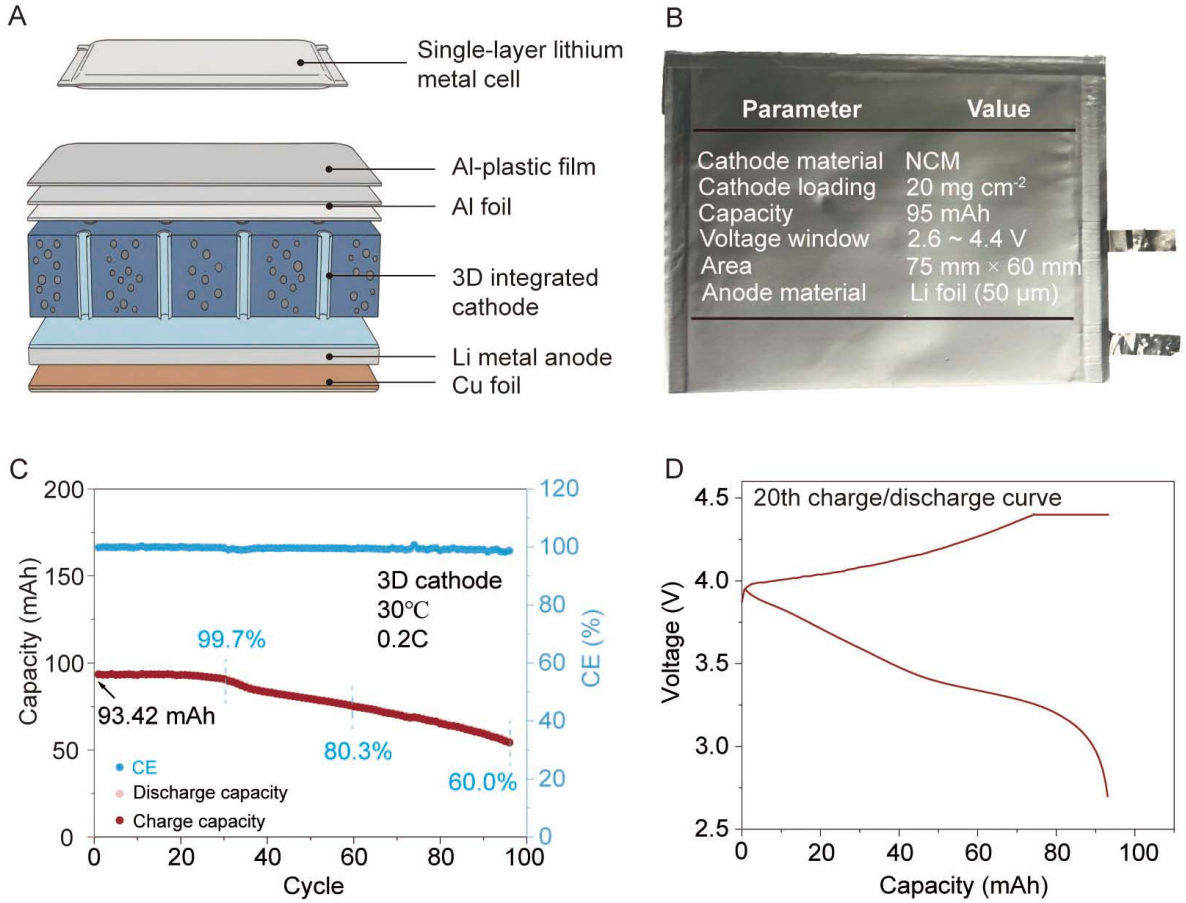

Figure 6. Practical application in a single-layer solid-state pouch cell. (A and B) Schematic configuration (A) and design parameters (B) of the assembled 95 mAh solid-state lithium metal cell featuring the integrated 3D cathode. (C and D) Cycling stability with Coulombic efficiency (C) and the representative 20th charge-discharge voltage profile (D) evaluated at 0.2 C and 30 °C.

minimal IR drop of only ~10-20 mV during each current pulse, in sharp contrast to the substantial resistance typically observed in high-loading unpatterned electrodes. Based on the GITT results, the lithium-ion diffusion coefficients (D_{Li^+}) were calculated and are summarized in Supplementary Figure 31. During the mid-to-late stages of lithiation/delithiation, the 3D cathode maintains D_{Li^+} values in the range of 10^{-9} to 10^{-11} cm^2 s^{-1}, which are approximately three orders of magnitude higher than those of the conventional thick electrode (10^{-13} to 10^{-14} cm^2 s^{-1}). These results quantitatively confirm that the vertical microchannels effectively facilitate Li^+ transport, mitigate localized concentration polarization, and enable more uniform ion flux within the high-loading cathode.

Practical demonstration in solid-state pouch cells

A large-format single-layer solid-state pouch cell (75 mm × 60 mm) was assembled to evaluate the scalability and practical applicability of this laser-engineered architecture. The pouch cell consists of the engineered cathode paired with a 50 μm thick lithium metal anode [Figure 6A]. The 3D integrated cathode was designed with a mass loading of 14.5 mg cm^{-2}, and the cell was operated within a voltage window of 2.6-4.4 V with a target capacity of 95 mAh [Figure 6B]. When tested at 30 °C and 0.2 C, the pouch cell delivered an initial discharge capacity of 93.42 mAh and an initial Coulombic efficiency of 99.7% [Figure 6C and D]. The corresponding charge-discharge profiles [Figure 6D] exhibit flat voltage plateaus and a small polarization gap. Notably, these favorable characteristics are maintained despite the challenging combination of enlarged pouch-cell format and high cathode mass loading. This result confirms that the 3D transport network can effectively homogenize local ion flux at the device level, thereby alleviating the severe mass-transfer limitations and macroscopic polarization commonly encountered in conventional large-format thick electrodes.

Driven by these macroscopic kinetic advantages, the 3D microchannel pouch cell exhibits improved electrochemical performance during practical cell operation. In comparison, the pouch cell employing the conventional thick cathode with a laminated electrolyte shows much larger polarization in the charge/discharge profiles, together with poor capacity utilization. Specifically, the conventional pouch cell delivers only 55.6 mAh, corresponding to 58.5% of the designed capacity of 95 mAh [Supplementary Figure 32]. In sharp contrast, the 3D microchannel pouch cell effectively alleviates polarization and enables higher areal-capacity utilization. During prolonged cycling, it retains 80.3% of its initial capacity after 60 cycles and maintains 60.0% capacity retention after 96 cycles. These results demonstrate that the 3D microchannel architecture helps bridge the gap between microstructural ion-transport design and practical high-loading solid-state pouch-cell implementation. Meanwhile, we note that the laser-processing parameters and the resulting electrode/electrolyte interfacial quality are important factors affecting pouch-cell performance. Further optimization of the laser-patterning process, including channel geometry, processing depth, and large-area uniformity, may provide an effective route to improving high-loading solid-state pouch cells and promoting the practical development of solid-state batteries.

CONCLUSIONS

In summary, we have developed a scalable 3D integrated cathode architecture that effectively addresses the mass-transfer limitations of high-loading solid-state lithium metal batteries. Through laser machining of vertical microchannels in dense NCM811 cathodes followed by infiltration of a solid polymer electrolyte, ion- and electron-transport pathways are spatially decoupled, enabling efficient charge transport throughout the electrode. Spatiotemporal simulations and operando impedance analysis demonstrate that these directional, low-tortuosity pathways reduce mass-transfer resistance and suppress detrimental concentration polarization. Consequently, the 3D cathode exhibits outstanding electrochemical reversibility, sustaining stable cycling over a wide voltage range of 2.7-4.5 V and delivering excellent rate performance up to 5.0 C, which are difficult to achieve with conventional thick cathodes. The practical applicability of this design is further validated in a 95 mAh single-layer solid-state pouch cell, which shows stable cycling and high Coulombic efficiency under practically relevant conditions. Overall, this structural-engineering strategy provides a general and effective framework for bridging the gap between material-level capability and device-level operation, offering a promising pathway toward next-generation high-energy-density solid-state batteries.

DECLARATIONS

Acknowledgments

The TEM study utilized resources from the Pico Center at the SUSTech Core Research Facilities, which is supported by the Presidential Fund and the Development and Reform Commission of Shenzhen Municipality.

Authors' contributions

Conceptualization, methodology, investigation, data curation, formal analysis, writing-original draft: Mu, Y.
Methodology, investigation, data curation, resources: Xu, C.; Li, M.; Huang, C.; Wu, Z.; Yang, L.; Feng, Y.; Chen, Z.; Lai, H.; Zou, Z.; Hu, H.; Zhang, G.
Formal analysis, project administration, supervision, writing-review and editing: Han, M.; An, L.
Conceptualization, methodology, formal analysis, project administration, supervision, writing-review and editing: Zeng, L.

Availability of data and materials

All data and materials supporting the results of this study are included in this article and Supplementary Materials. Further data are available from the corresponding authors upon reasonable request.

AI and AI-assisted tools statement

Not applicable.

Financial support and sponsorship

This work was financially supported by the Guangdong Major Project of Basic Research (No. 2023B0303000002), the Shenzhen Key Laboratory of Advanced Energy Storage (No. ZDSYS20220401141000001), and high-level special funds (No. G03034K001).

Conflicts of interest

All authors declared that there are no conflicts of interest.

Ethical approval and consent to participate

Not applicable.

Consent for publication

Not applicable.

Supplementary Materials

Supplementary Materials

REFERENCES

1. Zhao, Y.; Wang, D.; Gao, Y.; Chen, T.; Huang, Q.; Wang, D. Stable Li metal anode by a polyvinyl alcohol protection layer via modifying solid-electrolyte interphase layer. *Nano. Energy.* **2019**, *64*, 103893. DOI
2. Li, Z.; Weng, S.; Fu, J.; et al. Nonflammable quasi-solid electrolyte for energy-dense and long-cycling lithium metal batteries with high-voltage Ni-rich layered cathodes. *Energy. Storage. Mater.* **2022**, *47*, 542-50. DOI
3. Pan, K.; Zhang, L.; Qian, W.; et al. A flexible ceramic/polymer hybrid solid electrolyte for solid-state lithium metal batteries. *Adv. Mater.* **2020**, *32*, 2000399. DOI
4. Yang, J.; Li, M.; Sun, Z.; et al. Prolonging the cycling lifetime of lithium metal batteries with a monolithic and inorganic-rich solid electrolyte interphase. *Energy. Environ. Sci.* **2023**, *16*, 3837-46. DOI
5. Jabbari, V.; Yurkiv, V.; Rasul, M. G.; Phakatkar, A. H.; Mashayek, F.; Shahbazian-Yassar, R. In situ formation of stable solid electrolyte interphase with high ionic conductivity for long lifespan all-solid-state lithium metal batteries. *Energy. Storage. Mater.* **2023**, *57*, 1-13. DOI
6. Liu, L.; Shi, Y.; Liu, M.; et al. An ultrathin solid electrolyte for high-energy lithium metal batteries. *Adv. Funct. Mater.* **2024**, *34*, 2403154. DOI
7. Huang, H.; Liu, C.; Liu, Z.; et al. Functional inorganic additives in composite solid-state electrolytes for flexible lithium metal batteries. *Adv. Powder. Mater.* **2024**, *3*, 100141. DOI
8. Liang, W.; Liu, Y.; Dai, L.; et al. Strong dipole moments and increased charge transfer in polymer-based solid electrolyte enable wide-temperature solid-state lithium metal batteries. *Angew. Chem. Int. Ed.* **2025**, *64*, e202513604. DOI
9. Chen, Z.; Zhao, W.; Liu, Q.; et al. Janus quasi-solid electrolyte membranes with asymmetric porous structure for high-performance lithium-metal batteries. *Nano. Micro. Lett.* **2024**, *16*, 114. DOI PubMed PMC
10. Kang, Z.; Zhou, H.; Zheng, S.; et al. Exploring the failure mechanisms of quasi/all solid-state Li-ion batteries with Si-based electrodes. *Energy. Mater.* **2026**, *6*, 600024. DOI
11. Wu, H.; Jia, H.; Wang, C.; Zhang, J. G.; Xu, W. Recent progress in understanding solid electrolyte interphase on lithium metal anodes. *Adv. Energy. Mater.* **2020**, *11*, 2003092. DOI
12. Su, Y.; Rong, X.; Gao, A.; et al. Rational design of a topological polymeric solid electrolyte for high-performance all-solid-state alkali metal batteries. *Nat. Commun.* **2022**, *13*, 4181. DOI PubMed PMC
13. Wu, F.; Wen, Z.; Zhao, Z.; et al. Double-network composite solid electrolyte with stable interface for dendrite-free Li metal anode. *Energy. Storage. Mater.* **2021**, *38*, 447-53. DOI
14. Ye, G.; Hong, X.; He, M.; et al. All-solid-state lithium metal batteries with microdomain-regulated polycationic solid electrolytes. *Adv. Mater.* **2025**, *37*, 2417829. DOI
15. Liu, Y.; Shi, Z.; Yue, X.; et al. A transformative molecular muscle solid electrolyte. *J. Am. Chem. Soc.* **2025**, *148*, 1570-80. DOI

16. Zhang, Z.; Han, W. From liquid to solid-state lithium metal batteries: fundamental issues and recent developments. *Nano. Micro. Lett.* **2023**, *16*, 24. DOI PubMed PMC
17. Guo, C.; Du, K.; Tao, R.; et al. Inorganic filler enhanced formation of stable inorganic-rich solid electrolyte interphase for high performance lithium metal batteries. *Adv. Funct. Mater.* **2023**, *33*, 2301111. DOI
18. Jagger, B.; Pasta, M. Solid electrolyte interphases in lithium metal batteries. *Joule* **2023**, *7*, 2228-44. DOI
19. Nie, L.; Zhu, J.; Wu, X.; et al. A large-scale fabrication of flexible, ultrathin, and robust solid electrolyte for solid-state lithium-sulfur batteries. *Adv. Mater.* **2024**, *36*, 2400115. DOI
20. Sun, Y.; Li, J.; Xu, S.; Zhou, H.; Guo, S. Molecular engineering toward robust solid electrolyte interphase for lithium metal batteries. *Adv. Mater.* **2023**, *36*, 2311687. DOI
21. Chen, M.; Ma, C.; Ding, Z.; et al. Upgrading electrode/electrolyte interphases via polyamide-based quasi-solid electrolyte for long-life nickel-rich lithium metal batteries. *ACS. Energy. Lett.* , *2021*, 1280-9. DOI
22. Shan, T.; Ju, Z.; Xiao, D.; et al. Molecularly woven artificial solid electrolyte interphase. *Angew. Chem. Int. Ed.* **2025**, *137*, e202505056. DOI
23. Wang, Y.; Chen, S.; Li, Z.; Peng, C.; Li, Y.; Feng, W. In-situ generation of fluorinated polycarbonate copolymer solid electrolytes for high-voltage Li-metal batteries. *Energy. Storage. Mater.* **2022**, *45*, 474-83. DOI
24. Liu, S.; Ji, X.; Piao, N.; et al. An inorganic-rich solid electrolyte interphase for advanced lithium-metal batteries in carbonate electrolytes. *Angew. Chem. Int. Ed.* **2020**, *60*, 3661-71. DOI
25. Luo, P.; Zhang, Y.; Song, J.; et al. Understanding and mitigating acidic species in all-fluorinated electrolytes for a stable 572 Wh/kg lithium metal battery (LMB). *Energy. Storage. Mater.* **2025**, *78*, 104234. DOI
26. Yu, W.; Kang, Z.; Liu, Z.; et al. Physical-chemical dual networks enabled mechanically robust solid electrolytes for stress-strain regulation. *Energy. Storage. Mater.* **2026**, *85*, 104882. DOI
27. Yang, N.; Cui, Y.; Su, H.; et al. A chemically bonded ultraconformal layer between the elastic solid electrolyte and lithium anode for high-performance lithium metal batteries. *Angew. Chem. Int. Ed.* **2023**, *62*, e202304339. DOI
28. Yang, L.; Chu, Y.; Feng, Y.; et al. Breaking voltage limitations: triethyl phosphate-engineered PVDF-based electrolytes with dual-interphase stabilization for 4.7 V-class quasi-solid-state lithium metal batteries. *J. Am. Chem. Soc.* **2025**, *147*, 25940-9. DOI
29. Zhang, S.; Liang, T.; Wang, D.; et al. A stretchable and safe polymer electrolyte with a protecting-layer strategy for solid-state lithium metal batteries. *Adv. Sci.* **2021**, *8*, 2003241. DOI PubMed PMC
30. Boaretto, N.; Garcia-Calvo, O.; Cobos, M.; et al. Quasi-solid polymer electrolytes with binary and ternary salt mixtures for high-voltage lithium metal batteries. *Energy. Mater.* **2025**, *5*, 500040. DOI
31. Xu, D.; Su, J.; Jin, J.; et al. In situ generated fireproof gel polymer electrolyte with $Li_{6.4}Ga_{0.2}La_3Zr_2O_{12}$ as initiator and ion-conductive filler. *Adv. Energy. Mater.* **2019**, *9*, 1900611. DOI
32. Yang, Y.; Chen, H.; Wan, J.; et al. An interdigitated Li-solid polymer electrolyte framework for interfacial stable all-solid-state batteries. *Adv. Energy. Mater.* **2022**, *12*, 2201160. DOI
33. Ni, S.; Zhang, M.; Li, C.; et al. A 3D framework with Li_3N-Li_2S solid electrolyte interphase and fast ion transfer channels for a stabilized lithium-metal anode. *Adv. Mater.* **2022**, *35*, 2209028. DOI
34. Lu, P.; Wu, Y.; Wu, D.; et al. Rate-limiting mechanism of all-solid-state battery unravelled by low-temperature test-analysis flow. *Energy. Storage. Mater.* **2024**, *67*, 103316. DOI
35. Shin, S. S.; Kim, J.; Choi, S.; et al. Quantitative determination of lithium depletion during rapid cycling in sulfide-based all-solid-state batteries. *Chem. Commun.* **2021**, *57*, 3453-6. DOI